Materials Science and Engineering C 32 (2012) 1640–1647

Contents lists available at SciVerse ScienceDirect

Materials Science and Engineering C

journal homepage: www.elsevier.com/locate/msec

Amperometric glucose sensor based on enhanced catalytic reduction of oxygen using glucose oxidase adsorbed onto core-shell Fe_3O_4@silica@Au magnetic nanoparticles

Ai-Jun Wang [a,c], Yong-Fang Li [b], Zhong-Hua Li [c], Jiu-Ju Feng [a,c,*], Yan-Li Sun [c], Jian-Rong Chen [a]

[a] College of Geography and Environmental Science, College of Chemistry and Life Science, Zhejiang Normal University, Jinhua 321004, China
[b] College of Chemistry and Chemical Engineering, Henan Institute of Science and Technology, Xinxiang 453003, China
[c] Key Laboratory of Green Chemical Media and Reactions, Ministry of Education; School of Chemistry and Environmental Science, Henan Normal University, Xinxiang 453007, China

ARTICLE INFO

Article history:
Received 18 April 2011
Received in revised form 9 February 2012
Accepted 22 April 2012
Available online 29 April 2012

Keywords:
Fe_3O_4@silica@Au nanoparticles
Glucose biosensor
Electron transfer

ABSTRACT

Monodisperse Fe_3O_4 magnetic nanoparticles (NPs) were prepared under facile solvothermal conditions and successively functionalized with silica and Au to form core/shell Fe_3O_4@silica@Au NPs. Furthermore, the samples were used as matrix to construct a glucose sensor based on glucose oxidase (GOD). The immobilized GOD retained its bioactivity with high protein load of 3.92×10^{-9} mol·cm^{-2}, and exhibited a surface-controlled quasi-reversible redox reaction, with a fast heterogeneous electron transfer rate of 7.98 ± 0.6 s^{-1}. The glucose biosensor showed a broad linear range up to 3.97 mM with high sensitivity of 62.45 μA·mM^{-1} cm^{-2} and fast response (less than 5 s).

1. Introduction

Quantitative determination of glucose has been widely used in biochemistry, clinical chemistry, and food analysis [1–3]. Since Clark and coworkers reported the first electrochemical glucose biosensor, a lot of outstanding works have been reported about the design and construction of the bioelectronic devices [4], including biosensors [5,6], enzymatic reactors [7], and biofuel cells [8]. Most of the electrochemical glucose biosensors were developed based on the electrochemical oxidation of H_2O_2, which is liberated from glucose oxidation by glucose oxidase (GOD) in the presence of dissolved oxygen. Unfortunately, the amperometric determination of H_2O_2 requires a high anodic potential, which might induce unavoidable interferences from the other oxidizable species [9–12].

Electron transfer mediators such as Prussian blue [13,14] and ferrocene [15,16] were often used to avoid interferents, which transfer electrons between the redox centers of the GOD and underlying electrodes [17]. Nevertheless, the involved mediators in combination with GOD are usually general, rather than selective, facilitating electron transfer of the enzyme with the electrode, as well as a variety of interfering reactions [10,18,19]. Thus, mediator-free biosensors have attracted more and more attentions in the last several decades.

Since inflavin adenine dinucleotide (FAD, redox center) in GOD is deeply buried in the three-dimensional protein shells and difficult to access, well-defined direct electron transfer (DET) of the immobilized GOD is thus very difficult [5]. In the literature, only several outstanding works of quasi-reversible voltammograms of the GOD based biosensor were reported [20]. He et al. studied the DET of the GOD confined in the Au-dihexadecylphosphate composite at a graphite electrode [21]. Wang and coworkers studied the DET of the GOD adsorbed onto the graphene–CdS hybrid film at a glassy carbon electrode (GCE) [22]. Recently, the DET of the GOD on the carbon nanotubes was also investigated by a variety of groups [23–26]. To improve the performance of a mediator-free biosensor, it is significant to efficiently keep the enzyme with native structures and bioactivity on electrode surface, using different functional biocompatible nanomaterials.

Functional nanomaterials have received considerable attention because of their fundamental and technological interest and importance [27]. These functional nanomaterials can offer many advantages, including large surface-to-volume ratio, high surface reaction activity, and strong adsorption ability to immobilize some desired biomolecules such as enzyme, which might provide diverse platforms for electronic and optic (bio)sensors [28,29].

Magnetic materials (such as Fe_3O_4) have been synthesized by different methods [30] and used in biocatalysis [31,32], bio-labeling [33], and separation/purification of biomolecules [34]. However, only a few examples of well-defined Fe_3O_4 NPs with high dispersity have been constructed lately [35,36]. Among them, solvothermal synthesis is a popular method to prepare Fe_3O_4 nanostructures with well-defined morphologies [37–40]. Chen et al. constructed Fe_3O_4 nanoplates in the presence of poly(vinylpyrrolidone) molecules under solvothermal conditions [41]. Qiu and coworkers reported the round-biscuit-like Fe_3O_4 nanoparticles in large-scale by a simple solvothermal method [42]. In our work, monodisperse Fe_3O_4 were facilely prepared under solvothermal conditions.

* Corresponding author at: College of Geography and Environmental Science, College of Chemistry and Life Science, Zhejiang Normal University, Jinhua 321004, China. Tel./fax: +86 579 82282269.
E-mail address: jjfengnju@gmail.com (J-J. Feng).

0928-4931/$ – see front matter © 2012 Elsevier B.V. All rights reserved.
doi:10.1016/j.msec.2012.04.055

However, the bare iron oxides (Fe_3O_4 NPs) have high reactivity and easily undergo degradation upon direct exposing to certain environment, leading to poor stability. For example, Fe_3O_4 NPs with relatively small size would rapidly degrade upon exposing to aqueous solution [43]. Meanwhile, the Fe_3O_4 NPs have limited functional groups for selective binding. Consequently, a number of multifunctional Fe_3O_4 NPs are prepared, through further functionalization with enzymes, metal or other metal oxides to increase their functionality. For instance, capping Fe_3O_4 NPs with other materials (such as gold, silica, titania, and alumina) have been extensively studied [30].

Among them, coating the Fe_3O_4 particles with silica has attracted great interest in recent researches. The outer silica shells not only stabilize the functional magnetic particles in solution, but also provide silanol groups for secondary surface-mediated reactions [44]. Meanwhile, Au NPs are a kind of well-known biomaterials, because of their large ratio of surface area to volume, good biocompatibility, high catalytic activity, strong adsorption ability, well suitability, and excellent conductivity [45,46]. Thus, the Fe_3O_4@silica@Au NPs are a more attractive candidate, which provides a friendly microenvironment for efficient adsorption of enzyme (such as GOD), and improves the stability of the immobilized biomolecules in biological conditions.

In this work, monodisperse Fe_3O_4 NPs were initially synthesized under facile solvothermal conditions, and subsequently coated with silica and Au to form the Fe_3O_4@silica@Au hybrid NPs. The as-prepared samples were used as a matrix to construct a glucose sensor upon adsorption of the GOD, which showed direct electron communication of the GOD with underlying electrode, and exhibited high electrocatalytic ability towards glucose oxidation.

2. Materials and methods

2.1. Reagents

Glucose oxidase and $HAuCl_4$ were purchased from Sigma Chemical Co. (St. Louis, MO, USA). Polyethylene glycol (molecule weight (Mw): 620 000–630 000) was purchased from Kemiou Reagent Co. (Tianjin). Tetraethyl orthosilicate (TEOS), (3-aminopropy) triethoxysilane (APTES), cysteamine, polyethyleneimine (PEI, ca. 30% in water, Mw: 3000–3500), β-(D)-glucose, and sodium citrate were purchased from Crystal Pure Reagent Co., Ltd. (Shanghai). All other chemicals were of analytical grade and used without further purification. A permanent magnet was purchased from Asone Ltd. (Osaka, Japan). Phosphate solution (0.1 M) with different pH values were prepared by adjusting the ratio of potassium hydrogen phosphate with potassium dihydrogen phosphate. All aqueous solutions were prepared with twice-distilled water.

2.2. Preparation of Fe_3O_4 and Fe_3O_4@a-SiO_2 magnetic NPs

(a) Synthesis of Fe_3O_4 NPs: 0.78 g $FeCl_3 \cdot 6H_2O$ was dissolved in 16 mL ethylene glycol to form a clear solution, followed by mixing 1.31 g hexamethylene tetramine with 0.50 g polyethylene glycol together. The mixture was vigorously stirred for 30 min and then sealed in a Teflon-lined stainless-steel autoclave (20 mL capacity). The autoclave was kept at 200 °C for 4 h, and then naturally cooled to room temperature. The black products were washed several times with ethanol and dried at 60 °C for 6 h.

(b) Synthesis of the core–shell Fe_3O_4@SiO_2 NPs: the hybrid NPs were prepared via hydrolysis of TEOS in basic solution via Stöber's method [47] with minor modification. Briefly, 20 mg Fe_3O_4 NPs were dispersed into 10.0 mL anhydrous ethanol and sonicated for 10 min, followed by the addition of 18.8 mL isopropanol, 1.0 mL ammonia (24–28%), 3.6 mL water, and 60 μL TEOS under vigorous stirring for 2 h. The black products were sequentially washed with water and ethanol, and dried at 60 °C for 6 h.

(c) Aminopropyl terminated Fe_3O_4@SiO_2 NPs (denoted as Fe_3O_4@a-SiO_2) were achieved based on the previous method [50] with some modification. Briefly, 20 mg Fe_3O_4@SiO_2 NPs were dispersed into 30.0 mL ethanol and sonicated for 10 min, followed by the addition of 2.0 mL water. Then, 2.0 mL ammonia and 200 μL APTES were added into the above solution under vigorous stirring overnight. The final product was magnetically separated, completely washed with ethanol, and finally re-dispersed in 10 mL ethanol by sonication for 10 min. This coating formed an extra NH_2–silica layer.

2.3. Synthesis of Fe_3O_4@a-SiO_2@Au hybrid NPs

(a) The introduction of positive charges onto the surface of the Fe_3O_4@a-SiO_2 NPs were implemented by adding diluted HNO_3 solution (by mixing 0.05 mL 6 M HNO_3 with 20 mL ethanol) into the ethanolic dispersion of the Fe_3O_4@a-SiO_2 NPs and vigorously stirred for 4 h based on Wu's method [48].

(b) The Fe_3O_4@a-SiO_2@Au NPs were prepared via sonolysis of a mixture of $HAuCl_4$ and Fe_3O_4@a-SiO_2 NPs with further drop-addition of sodium citrate. The prepared procedures were shown in Scheme 1.

2.4. Preparation of the GOD/Fe_3O_4@a-SiO_2@Au NPs modified electrodes

Before modification, a glassy carbon electrode (GCE) was polished with ultrafine emery paper until a smooth surface was obtained and cleaned with water. After that, the GCE was immersed into the 1% PEI (in 0.5 M NaCl) solution and 3 $mg \cdot mL^{-1}$ poly(styrenesulfonate) (PSS, Mw: 7000) solution for 30 min, respectively. Finally, the electrode was thoroughly washed with water and dried by nitrogen, denoted as p-GCE (i.e. a bare GCE was successively coated with PEI and PSS).

Prior to use, 8 mg Fe_3O_4@a-SiO_2@Au NPs were dispersed into 1.0 mL water to form a stable black suspension under ultrasonic stirring for 30 min (the concentration of the Fe_3O_4@a-SiO_2@Au is about 8 $mg \cdot mL^{-1}$). Then, an aliquot of the suspension (8.0 μL) was evenly dropped onto the p-GCE surface and allowed to dry at 4 °C. Then, the Fe_3O_4@a-SiO_2@Au modified electrodes were immersed into the 50 mM cysteamine (Cys) solution containing 0.5 M NaCl to functionalize the Au NPs by self-assembly, similar to our previous study on cytochrome c adsorbed on a mercaptohexanoic acid (MUA)-coated Ag [49] and Ag–silica–Au [50] devices. Next, the Cys/Fe_3O_4@a-SiO_2@Au modified electrode was put into 10 $mg \cdot mL^{-1}$ GOD solution including 5 mM phosphate solution (pH 7.0) for 4 h. The resultant modified electrode is denoted as the GOD/Cys/Fe_3O_4@a-SiO_2@Au/p-GCE. The preparation procedures of the GOD/Cys/Fe_3O_4@a-SiO_2@Au/p-GCE were shown in Scheme 2.

In addition, the Cys/Fe_3O_4@a-SiO_2@Au/p-GCE, Fe_3O_4@a-SiO_2@Au/p-GCE, and p-GCE electrodes were prepared as control electrodes.

2.5. Characterization

X-ray diffraction (XRD) analysis was performed with a Rigaku Dmax-2000 diffractometer using Cu Kα radiation. Transmission electron microscopy (TEM) was performed using a field emission TEM operating at 200 kV to measure the particle size and shape. The infrared absorption spectra of the samples were recorded on a Fourier transform infrared spectrometer (model 1615, Perkin-Elmer, Norwalk, CT). UV–vis absorption spectra were acquired with a UV-2450 spectrophotometer. Dynamic light scattering (DLS) measurement was carried out with a DLS spectrometer (Malvern, Nano ZS, ZEN3600). The samples were strongly ultrasonicated for 30 min, and then the DSL experiments were performed quickly at room temperature. Electrochemical experiments were conducted on a CHI 660D electrochemical workstation. All the experiments were performed using a

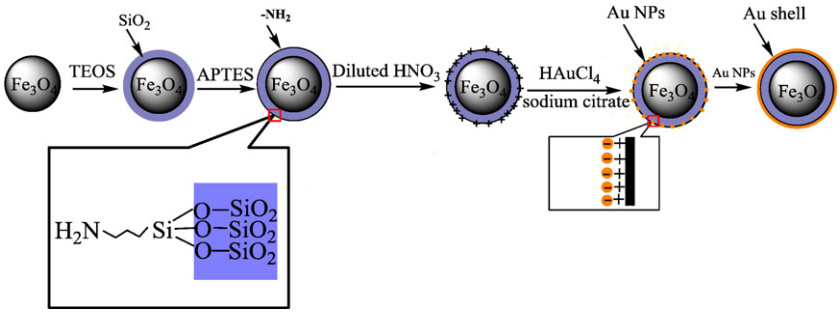

Scheme 1. Schematic illustration of the procedure for the preparation of the Fe_3O_4@a-SiO_2@Au NPs.

conventional three-electrode system, including the bare or modified electrode as the working electrode, a saturated calomel electrode (SCE) as the reference electrode, and a platinum wire as the counter electrode. Electrochemical impedance spectroscopy (EIS) experiments were performed in 0.1 M KNO_3 solution containing 5.0 mM $Fe(CN)_6^{3-}$/$Fe(CN)_6^{4-}$ (1:1) at room temperature, using an alternating current voltage of 5.0 mV. The open circuit potential was about 180 mV in the frequency range of 10^{-2}–10^5 Hz.

3. Results and discussion

3.1. Synthesis of the Fe_3O_4 NPs

The preparation of the Fe_3O_4 NPs was conducted by adding hexamethylene tetramine into $FeCl_3$ solution that was dissolved in polyethylene glycol solution. In this process, ethylene glycol is used as a protective agent to prevent the agglomeration of the formed Fe_3O_4 NPs, and also as a strong reducing agent with a relatively high boiling point [51]. However, the Fe^{3+} ion could not be reduced to Fe_3O_4 without hexamethylene tetramine. Therefore, hexamethylene tetramine is crucial for the synthesis of the Fe_3O_4 NPs. Here, hexamethylene tetramine would be hydrolyzed into HCHO and $NH_3 \cdot H_2O$. The formed HCHO plays an important role in the ethylene glycol mediated reduction of the Fe^{3+} ion, while the generated $NH_3 \cdot H_2O$ provides alkaline media to promote the hydrolysis of the Fe^{3+} ion. Eventually, their synergetic effects cause the hydrolysis products of the Fe^{3+} ion to form the Fe_3O_4 NPs.

3.2. XRD spectra

The typical XRD patterns of the samples were provided to characterize their specific structures (Fig. 1). As can be seen, all the diffraction peaks (marked in blue) are well indexed to the cubic structure of the Fe_3O_4 (JCPDS 79-0419) with a lattice constant of $a = 8.391$ Å (curve a). Moreover, the peaks are strong and sharp, revealing good crystallization of the as-prepared Fe_3O_4 NPs. Similar characteristic peaks are observed for the Fe_3O_4 NPs after coated with pure SiO_2 (Fe_3O_4@SiO_2, curve b) and aminopropyl terminated SiO_2 (Fe_3O_4@a-SiO_2, curve c). These results demonstrate the crystallized Fe_3O_4 NPs have good stability. However, additional peaks are appeared at 38.6°, 44.7°, 64.8°, and 77.7° (marked in red). These peaks are ascribed to the (111), (200), (220), and (311) planes, respectively. These values are in good agreement with those in the literature for the face-centered-cubic gold (JCPDS No. 04-0784), respectively [46]. Meanwhile, some peaks from the Fe_3O_4 NPs become weaker or even invisible. These results demonstrate that the generated Au NPs are decorated on the surface of the Fe_3O_4@a-SiO_2 NPs.

3.3. TEM images

The morphologies of the samples were checked by TEM experiments. The average diameter of the as-prepared Fe_3O_4 particles is about 80 nm (Fig. 2A). After treatment by the modified Stöber's reaction, the Fe_3O_4 particles are completely covered with a uniform transparent silica layer (Fig. 2B). Furthermore, the particle size is roughly increased to 120 nm. That is, the thickness of the SiO_2 shell is about 20 nm. After reducing the adsorbed $AuCl_4^-$ ion by citrate, many Au NPs with the average size of 15 nm are decorated on the surface of the Fe_3O_4@a-SiO_2 particles (Fig. 2C, Fig. S1 and S2, Supporting Information). Thus, the Fe_3O_4@a-SiO_2@Au NPs are obtained. Since the amine groups on the a-SiO_2 surface preferentially bind noble metals such as Au NPs, instead of other species [52]. Moreover, the DSL experiments further confirm that the sizes of the Fe_3O_4, Fe_3O_4@SiO_2, and Fe_3O_4@a-SiO_2@Au NPs were increased with coating layers (Fig. S2, Supporting Information). In addition, some Au NPs are also observed (Fig. S2D), since Au NPs have been desorbed after treatment with strong ultrasonication for 30 min.

3.4. Fourier transform infrared (FT-IR) and UV–vis spectra

The FT-IR spectra of the Fe_3O_4, Fe_3O_4@SiO_2, Fe_3O_4@a-SiO_2, and Fe_3O_4@a-SiO_2@Au NPs are presented (Fig. 3A). For all samples, the absorption peak at 592 cm^{-1} is observed (Fig. 3A, curve a), corresponding to the Fe—O vibration from the magnetite phase [30]. The absorption bands at 1220, 1094, 804, and 471 cm^{-1} are detected on the Fe_3O_4@SiO_2 (Fig. 3A, curve b) and Fe_3O_4@a-SiO_2 (Fig. 3A, curve c) spectra, which are ascribed to the characteristic peaks of the SiO_2 layer. These results demonstrate the formation of silica shells around the Fe_3O_4 particles.

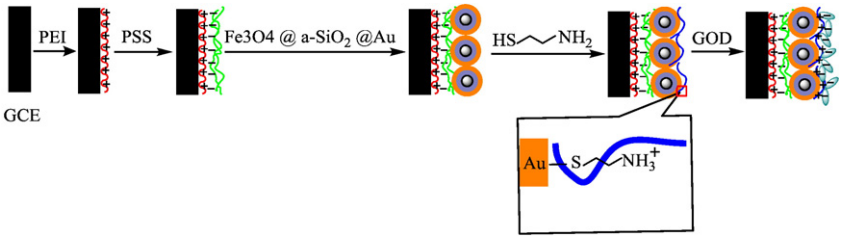

Scheme 2. Schematic illustration of the procedure for the preparation of the GOD/Cys-HL/ Fe_3O_4 @a-SiO_2 @Au /PSS/PEI/GCE.

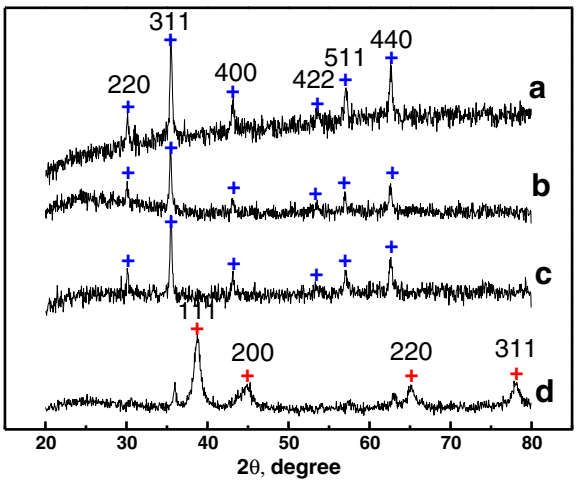

Fig. 1. The XRD patterns of synthesized Fe_3O_4 (a), Fe_3O_4 @SiO_2(b), Fe_3O_4@a-SiO_2 (c), and Fe_3O_4 @a-SiO_2NPs@Au (d) particles.

Moreover, the absorption peaks within 2800–3025 cm^{-1} are associated with the methylene groups of the Fe_3O_4@a-SiO_2 particles. These results indicate the attachment of amine groups onto the surface of the Fe_3O_4 NPs. Moreover, the aminopropyl functionalization of the silica layer is further evidenced by the typical bands at 3361, 1572, 1498, and 692 cm^{-1}. When the Fe_3O_4@a-SiO_2 NPs are further functionalized with Au NPs, similar observations are obtained (Fig. 3A, curve d), in comparison with those of the Fe_3O_4@a-SiO_2 (Fig. 3A, curve c). This is due to nearly no absorption of the Au NPs detected in the infrared region.

These samples (dispersed in ethanol) were further characterized by UV–vis experiments (Fig. 3B). The absorbance intensity decreased monotonically with the increase of the light wavelength from 400 to 900 nm, in good agreement with the results in the literature [53]. Moreover, the surface plasmon peaks of the Fe_3O_4, Fe_3O_4@SiO_2, and Fe_3O_4@a-SiO_2 disappeared. However, an extra surface plasmon peak is clearly observed at 580 nm for the Fe_3O_4@a-SiO_2@Au ethanol solution, which is attributed to the surface plasmon resonance bands of the decorated Au NPs. This value is different from that of the Au NPs in aqueous solution with a value of 515 nm (Fig. 3B, curve a) and that reported previously with a value of 520 nm [54].

It is well known that the increase of the Au particle size would cause an absorption peak shift in red direction, owing to the collective oscillations of the free electrons [55]. On the basis of the Mie theory, the shift of the surface Plasmon peak is directly associated with the particle size, stabilizing ligand, and solvent dielectric constants for the Au NPs. Similar observation has been reported for the Au-coated iron oxide NPs [56].

3.5. Electrochemical impedance spectroscopy

The Nyquist plots show the typical characters for a cell in which polarization is due to a combination of the electron transfer and diffusion processes [57]. As shown in Fig. 4, the Fe_3O_4/p-GCE exhibits a larger diameter of the semicircle in the Nyquist plot (Fig. 4, curve b), compared to that of the p-GCE (a bare GCE successively coated with PEI and PSS, curve a). This reveals a drastic increase in the electron-transfer resistance (R_{et}), since the deposited composite hinders the electron transfer from the redox probe of the $Fe(CN)_6^{3-/4-}$ to the electrode. Furthermore, the R_{et} of the Fe_3O_4@SiO_2/p-GCE (curve e) and Fe_3O_4@a-SiO_2/p-GCE (curve f) is consequently increased obviously, compared to that of the Fe_3O_4/p-GCE. It means that pure SiO_2 and a-SiO_2 are formed around the Fe_3O_4 NPs outside, respectively. However, the R_{et} decreases remarkably in the case of the Fe_3O_4@a-SiO_2@Au/p-GCE (curve c). It demonstrates that the generated Au NPs with good

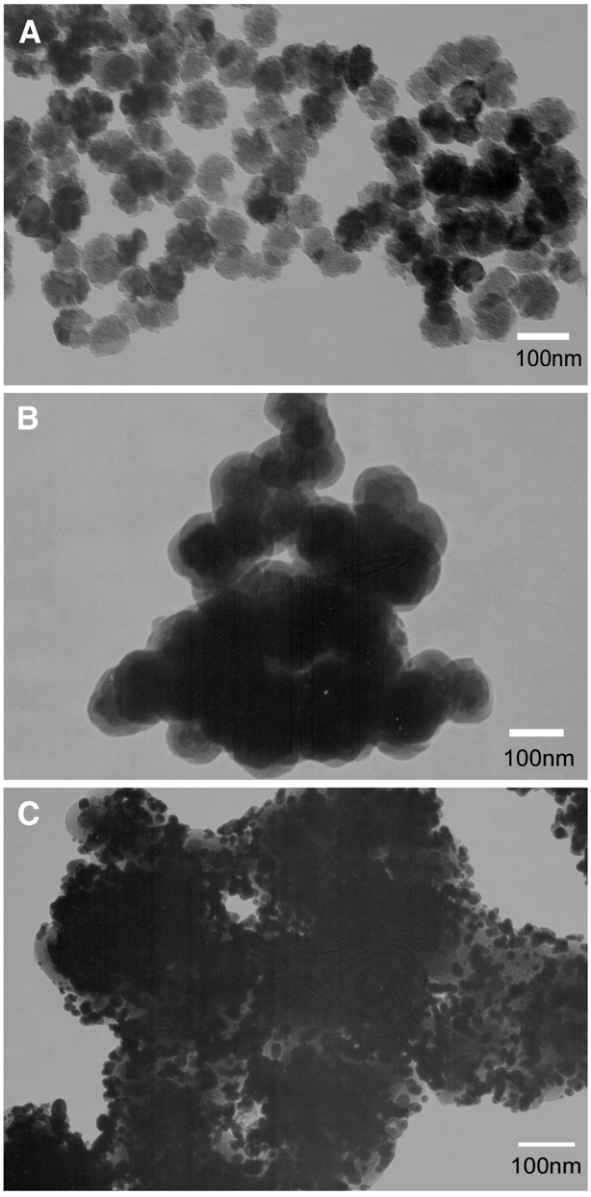

Fig. 2. TEM images of the Fe_3O_4(A), Fe_3O_4@SiO_2 (B), and Fe_3O_4@a-SiO_2@Au (C) particles.

electrical conductivity and thereby makes the electron transfer easier. After the GOD efficiently absorbed onto the Cys/Fe_3O_4@SiO_2@Au/p-GCE, the corresponding R_{et} greatly increases again (curve d). It suggests that the GOD is steadily adsorbed onto the Cys/Fe_3O_4@SiO_2@Au/p-GCE, causing the inhibition of the electron transfer of the redox couple.

3.6. The DET of the immobilized GOD

The electrochemistry of the GOD was tested by cyclic voltammetry in anaerobic phosphate solution (pH 7.4) at 100 $mV \cdot s^{-1}$. After adsorption of the GOD onto the Cys/Fe_3O_4@a-SiO_2@Au electrode (Fig. 5A, curve a), a pair of well-defined and nearly symmetric redox peaks is observed at −0.21 V and −0.40 V, respectively, which is ascribed to the FAD in GOD [23–26]. The peak potential separation (ΔE_p) is about 190 mV. Meanwhile, the apparent formal potentials ($E^{\circ\prime}$, which is calculates as $E^{\circ\prime} = (E_{p,a} + E_{p,c})/2$) is -300 ± 10 mV. The smaller ΔE_p and more positive $E^{\circ\prime}$ indicate faster electron communication in our case, compared to those before [22]. Thus, the Cys/Fe_3O_4@a-

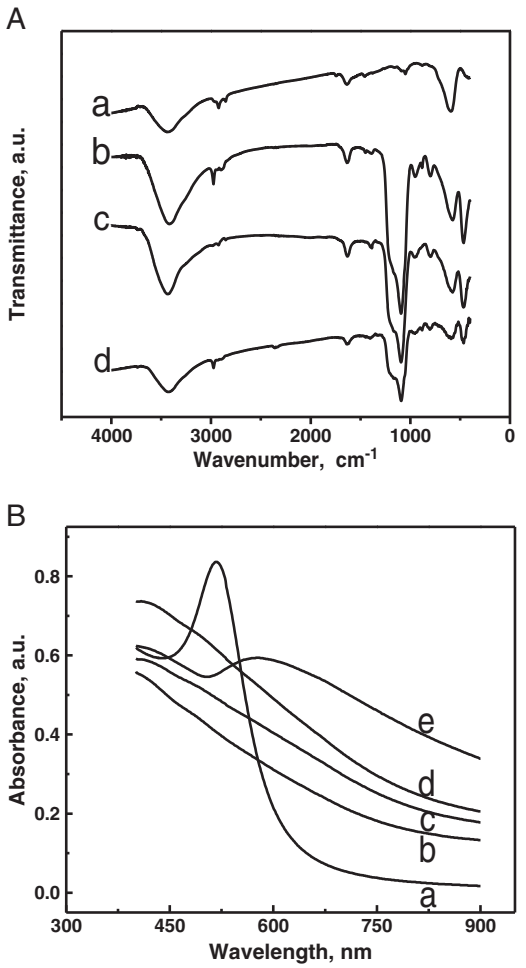

Fig. 3. (A) FT-IR spectra of the Fe_3O_4 (a), Fe_3O_4@SiO_2 (b), Fe_3O_4@a-SiO_2 (c), and Fe_3O_4@a-SiO_2@Au (d) particles. (B) UV–vis spectra of the Au NPs solution (a), Fe_3O_4 (b), Fe_3O_4@SiO_2 (c), Fe_3O_4@a-SiO_2 (d), and Fe_3O_4@a-SiO_2@Au (e) particles.

SiO_2@Au NPs effectively promote the DET between the GOD and the electrode, resulted from the decrease of the overpotentials.

For comparative study, the cyclic voltammograms (CVs) of the GOD were recorded at the control electrodes including the p-GCE (PEI/PSS/GCE), Fe_3O_4/p-GCE, Fe_3O_4@SiO_2/p-GCE, Fe_3O_4@a-SiO_2/p-GCE, and

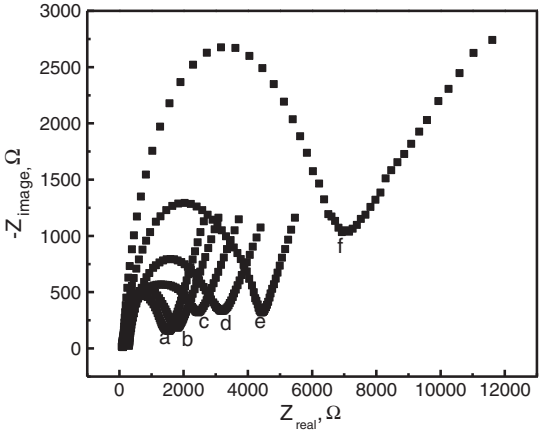

Fig. 4. EIS of the bare (a), Fe_3O_4 (b), Fe_3O_4@a-SiO_2@Au (c), GOD/Cys/Fe_3O_4@-SiO_2@Au (d), Fe_3O_4@SiO_2 (e), and Fe_3O_4@a-SiO_2 (f) modified p-GCE in 0.1 M phosphate solution (pH 7.4) containing 5 mM $K_3Fe(CN)_6$/$K_4Fe(CN)_6$.

Fe_3O_4@a-SiO_2@Au/p-GCE. Evidently, nearly no peaks are observed under the same conditions (data not shown). For the p-GCE, successively coated with PEI and PSS, the negative charged surface is not good to adsorb negative charged GOD in neutral phosphate solution (isoelectric point of GOD is 4.2), owing to electrostatic repulsion. Moreover, the DET does not realize after drop-casting of the Fe_3O_4, Fe_3O_4@SiO_2, or Fe_3O_4@a-SiO_2 NPs, due to their poor conductivity. Similarly, the DET is still inaccessible on the Fe_3O_4@a-SiO_2@Au NPs modified electrode.

The effect of the scan rate (v) on the GOD/Cys/Fe_3O_4@a-SiO_2@Au electrode had been examined. Fig. 5A shows the CVs of the electrode in a N_2-saturated phosphate solution. With the increase of the scan rate, the anodic peak potentials of the GOD positively shift, while the cathodic peak potentials shift to a negative direction. Nevertheless, the $E°'$ is almost constant. Here, the cathodic peak currents (I_{pc}) and anodic peak currents (I_{pa}) increase linearly within 10–100 $mV \cdot s^{-1}$ (Fig. 5B), in accordance with the equation of $I_p = nFQv/4RT$, where n is the number of electron transfer, F is the Faraday constant (96485 $C \cdot mol^{-1}$), R is the universal gas constant (8.314 $J \cdot K^{-1} \cdot mol^{-1}$), and T is the absolute temperature, respectively [20]. The charge consumed in coulombs (Q, i.e. the cathodic peak area) keeps nearly unchanged at different scan rates. All the results demonstrate that the redox reaction of the GOD is a quasi-reversible surface-controlled electrochemical process [22–26].

Meanwhile, the apparent surface concentration of the electroactive GOD (Γ, $mol \cdot cm^{-2}$) can be estimated to be about 3.92×10^{-9} $mol \cdot cm^{-2}$ ($n = 2$) based on Laviron equation [58], much larger than the theoretical value of 2.86×10^{-12} $mol \cdot cm^{-2}$ for the monolayer of the GOD [59], and those reported for the $(GOD/PEI)_3$ film of 4.7×10^{-10} $mol \cdot cm^{-2}$ [24], the GOD/Au film of $9.89 \pm 0.6 \times 10^{-12}$ $mol \cdot cm^{-2}$ [20], the GOD–Au nano–DHP of 7.82×10^{-12} $mol \cdot cm^{-2}$ [21], and the GOD-IL-GNP-ILSWNT of 1.27×10^{-10} $mol \cdot cm^{-2}$ [60].

The kinetics of the heterogeneous electron transfer was analyzed using the model of Laviron equation [61] for a surface-controlled electrode process. Since the $\Delta E_p < 200$ mV, the apparent electron transfer rate constant (k_s) can be obtained below. Taking the electron rate coefficient (α) of 0.5, the average k_s is 7.98 ± 0.6 s^{-1} in the scan range from 10 to 100 $mV \cdot s^{-1}$. This value is larger than those of the Nafion/GOD–GNPs/GCE (1.30 s^{-1}) [62], the GOD/TPSP-ZnO/ Nafion/GCE (7.5 ± 0.4 s^{-1}) [63], and the GOD-IL-GNP-ILSWNT/GCE (2.12 s^{-1}) [60].

The influence of the pH in the phosphate solution is also investigated (Fig. 5C). Obviously, the peak currents and $E°'$ of the GOD strongly depend on the pH values. When the pH values shift from 3.4 to 7.9, the maximum peak currents are observed in the optimal pH range from 6.5 to 7.5. The decreased peak currents at high pH might be ascribed to the increase of the electron transfer distance between the protein active center and the hybrid composites, while the decrease of the currents at low pH might be due to the denaturation of the adsorbed GOD, which results from the dissociation of FAD group when the pH is below 4.35 [20]. Meanwhile, an increase in the pH values causes a negative shift in both anodic and cathodic peak potentials of the GOD, indicating the protons participate in the electrode reaction. With the increase of the pH, the $E°'$ changes linearly with a slope of -55.1 $mV \cdot pH^{-1}$ ($r = 0.998$) (Fig. 5D), similar to the theoretical value of -58.6 $mV \cdot pH^{-1}$ [64] at 22 °C for two-proton coupled with two-electron redox reaction process.

3.7. Electrocatalytic behavior of the GOD/Cys/Fe_3O_4@a-SiO_2@Au/p-GCE

The influence of the dissolved oxygen on the electrochemical behavior of the GOD was investigated in air-saturated and air-free phosphate solution (Fig. S3, Supporting Information). Obviously, the cathodic current of the GOD is higher in air-saturated phosphate solution (curve a) than that without oxygen (curve b). It indicates that the dissolved oxygen undergoes catalytic reduction. Similar observations have been reported previously [20–26].

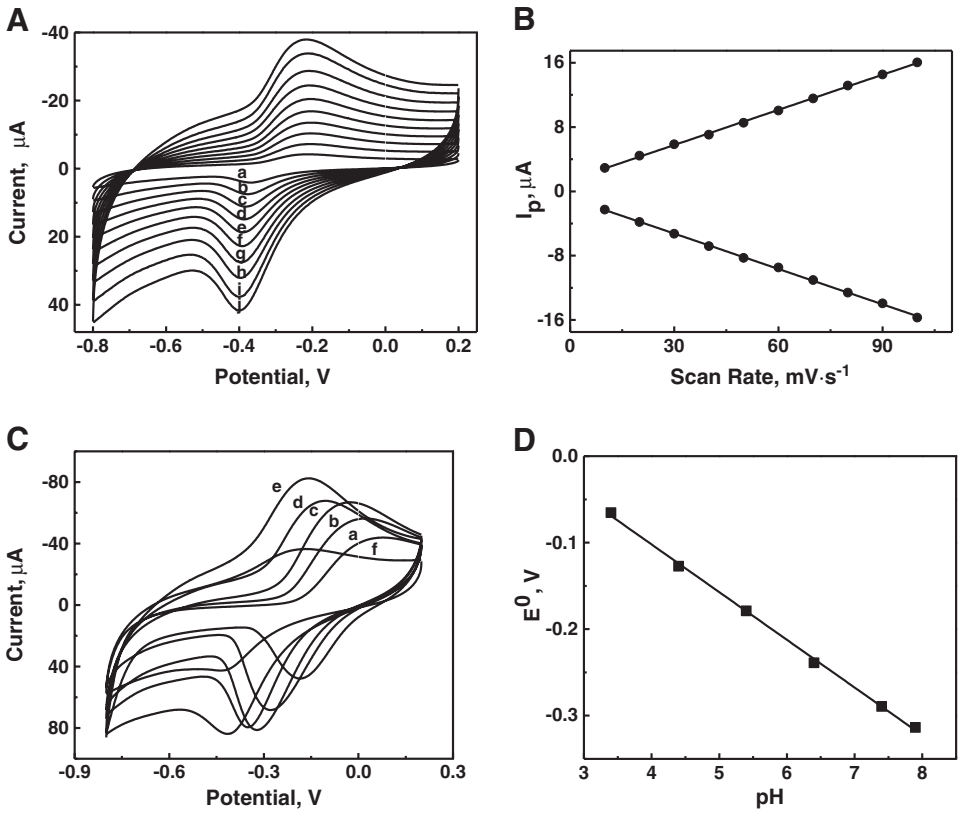

Fig. 5. (A) Cyclic voltammograms of the GOD/Cys/Fe_3O_4@a-SiO_2@Au/p-GCE with different scan rates (a–j): 10, 20, 30, 40, 50, 60, 70, 80, 90, and 100 mV·s^{-1} (from inner to outer) in 0.1 M phosphate solution (pH 7.4). (B) Relationship of the scan rates with the cathodic or anodic peak currents. (C) Cyclic voltammograms of the GOD/Cys/Fe_3O_4@a-SiO_2@Au/p-GCE with different pH values of (a–f): 3.4, 4.4, 5.4, 6.4, 7.4, and 7.9 in 0.1 M phosphate solution at 100 mV·s^{-1}. (D) Plot of the formal potential of the GOD/Cys/Fe_3O_4@a-SiO_2@Au/p-GCE as a function of pH values.

More importantly, when β-(D)-glucose was present in the air-saturated solution, the cathodic peak currents decrease with the increase of the glucose concentration (curve c). As known, the GOD can catalyze the glucose oxidation by oxygen to produce gluconolactone and hydrogen peroxide (H_2O_2). Oxygen is used as the electron acceptor. This enzyme-catalyzed reaction occurs as follows according to Eq. (1):

$$\mathrm{GOD(FADH_2)} + \mathrm{O_2} \rightarrow \mathrm{GOD(FAD)} + \mathrm{H_2O_2} \quad (1)$$

$$\beta\text{—(D)—glucose} + \mathrm{GOD(FAD)} \rightarrow \mathrm{GOD(FADH_2)} + \text{gluconolactone} \quad (2)$$

However, the existence of glucose is not good for the electrocatalytic reaction, since another enzyme-catalyzed reaction coexists between the oxidized form of GOD, GOD(FAD), and glucose (Eq. (2)). Consequently, the catalytic currents become smaller [24,20,64,65]. Here, comparative investigations were performed using the control electrodes without GOD, including the p-GCE, Fe_3O_4/p-GCE, Fe_3O_4@SiO_2/p-GCE, Fe_3O_4@a-SiO_2/p-GCE, Fe_3O_4@a-SiO_2@Au/p-GCE, and Cys/Fe_3O_4@a-SiO_2@Au/p-GCE (Fig. S4, Supporting Information). The oxygen reduction peak potential at the p-GCE is about −0.47 V, slightly lower than that at a bare GCE (−0.51 V). After drop-casting of the Fe_3O_4 NPs (Fe_3O_4/p-GCE), the oxygen reduction peak potential shifts positively to −0.38 V, accompanied with the increase of the peak currents. After the Fe_3O_4 NPs are further coated with pure or amine-terminated silica as shells, the oxygen reduction peak potential shifts back to −0.47 V. However, when the Au shells are coated around the Fe_3O_4@a-SiO_2 NPs, a largely enhanced catalytic current for oxygen reduction is observed with a peak potential of −0.14 V. This is a reflection of the pronounced catalytic activity of the amino-terminated Au NPs with respect to oxygen reduction. Thus, the Cys/Fe_3O_4@a-SiO_2@Au/p-GCE demonstrates a superior catalytic ability towards oxygen reduction. At the same time, it is an excellent matrix for the immobilization of biomolecules, such as GOD in our system.

The performance of the GOD/Cys/Fe_3O_4@a-SiO_2@Au/p-GCE towards glucose was further illustrated. Fig. 6A displays the relationship of the decreased currents of the GOD with glucose. The decrease of the currents is linear with glucose concentration up to 3.97 mM (Fig. 6B). The linear regression equation is ΔI_p (μA) = −0.49 + 6.68 C (mM) (r = 0.999). Furthermore, the slope of this plot is about 6.68 μA·mM^{-1}, which is subsequently divided by the electrode area (0.1070 cm^2), and finally obtained the sensitivity with a value of 62.45 μA·mM^{-1}·cm^{-2}. Furthermore, with successive addition of glucose, a typical current–time plot is obtained using the applied potential of −0.4 V (Fig. S5, Supporting Information). The catalytic response is very fast to reach a stable value within 5 s. The detection limit is about 0.23 μM at signal-to-noise ratio of 3. As shown in Fig. 6, the decreased currents are initially linear with glucose, and then become nonlinear, and finally reach a plateau, showing a typical Michaelis–Menten kinetic mechanism [66]. The apparent Michaelis–Menten constant (K_m^{app}), which is generally used to evaluate the catalytic activity of the immobilized enzyme, can be calculated according to Lineweaver–Burk equation [67]. In this work, the K_m^{app} of the GOD is about 13.02 mM, which is compared with some earlier GOD modified electrodes (Table S1, Supporting Information). Evidently, the resulting electrode shows good electrocatalytic performance for glucose determination, such as high sensitivity, fast response, wide linear range, and low detection limit.

The effects of some common interfering substances, such as uric acid and ascorbic acid, were investigated (Fig. 7). Clearly, no obvious interference of 0.01 mM uric acid or ascorbic acid is observed in the CVs in the presence of 0.4 mM glucose, reflecting high selectivity of the resulting sensor.

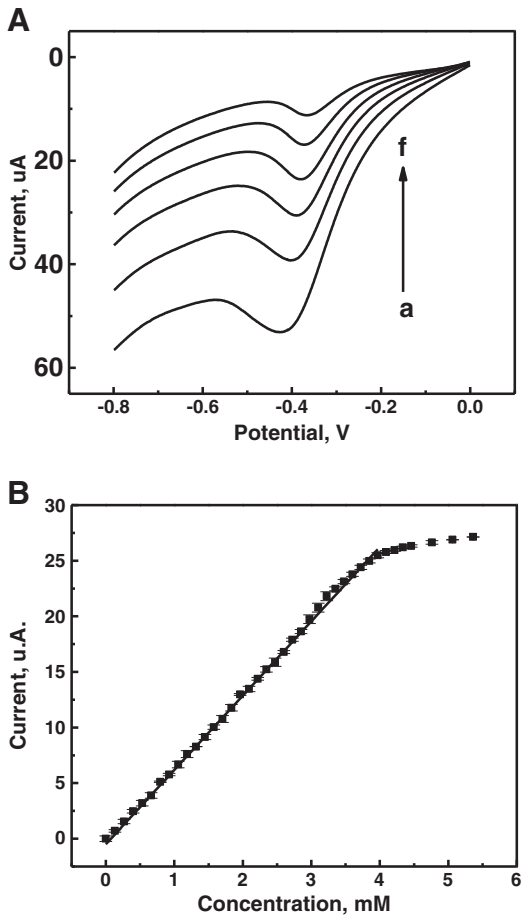

Fig. 6. (A) Linear sweep voltammograms of the GOD/Cys/Fe_3O_4@a-SiO_2@- Au/p-GCE in 0.1 M air-saturated phosphate solution (pH 7.4) containing 0, 0.66, 1.32, 1.96, 2.60, and 3.23 mM glucose at 100 mV·s^{-1} (from bottom to top). (B) Plot of the decreased reduction peak currents (ΔI_{pc}) vs. glucose concentration.

The stability and reproducibility were also evaluated by cyclic voltammetry. The catalytic currents of the GOD decrease with a value of 1.61% after continuously scanning 50 cycles, indicating good stability of the resulting sensor. In addition, the relative standard deviation (RSD) of the electrode response toward 0.13 mM glucose is 5.75% for five successive measurements. And the RSD for the detection of 0.4 mM glucose is 5.46% with five sensors prepared independently. These results suggest good reproducibility of the resulting sensor.

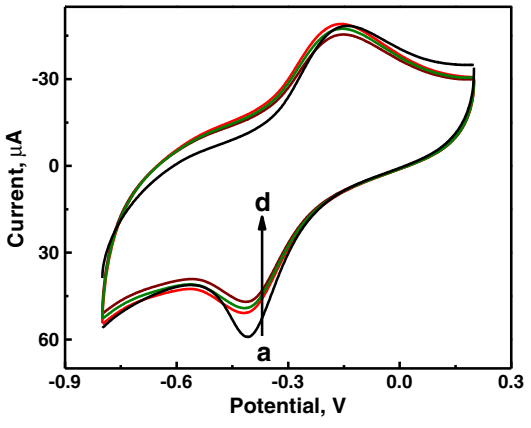

Fig. 7. Cyclic voltammograms of the GOD/Cys/Fe_3O_4@a-SiO_2@Au/p-GCE in 0.1 M air-saturated phosphate buffer solution (pH 7.4) without (a) and with 0.40 mM glucose (b), 0.40 mM glucose containing 0.01 mM UA (c), or 0.01 mM AA (d). Scan rate: 100 mV·s^{-1}.

4. Conclusions

In this study, the Fe_3O_4@silica@Au magnetic hybrid NPs with core-shell structures were prepared and used to construct a glucose sensor. The DET of the GOD/Cys/Fe_3O_4@a-SiO_2@Au/p-GCE was realized and the GOD retained its good bioactivity. The practical performance of the resulting sensor exhibited a broad linear range, fast response, good selectivity and stability. Therefore, the resulting sensor represents a practical approach towards the development of protein-based bioelectronic devices in which a high and stable protein load is essential.

Acknowledgements

This work was financially supported by the Natural Science Foundation of China (nos. 20805011, 20905021, and 21175218), the Foundation of the Ministry of Education of China for Returned Scholars (A.J. Wang and J.J. Feng), and the opening funding of State Key Laboratory of Analytical Chemistry for Life Science of Nanjing University (SKLACLS1107 for J.J. Feng).

Appendix A. Supplementary data

Supplementary data to this article can be found online at http://dx.doi.org/10.1016/j.msec.2012.04.055.

References

[1] J. Wang, Chem. Rev. 108 (2007) 814–825.
[2] Y. Lin, F. Lu, Y. Tu, Z. Ren, Nano Lett. 4 (2003) 191–195.
[3] J.R. Castle, W.K. Ward, J. Diabetes Sci. Technol. 4 (2010) 221–225.
[4] K.Y. Kwon, J. Youn, J.H. Kim, Y. Park, C. Jeon, B.C. Kim, Y. Kwon, X. Zhao, P. Wang, B.I. Sang, J. Lee, H.G. Park, H.N. Chang, T. Hyeon, S. Ha, H.-T. Jung, J. Kim, Biosens. Bioelectron. 26 (2010) 655–660.
[5] R. Wilson, A.P.F. Turner, Biosens. Bioelectron. 7 (1992) 165–185.
[6] J. Yang, S. Deng, J. Lei, H. Ju, S. Gunasekaran, Biosens. Bioelectron. 29 (2011) 159–166.
[7] S.-J. Li, C. Wang, Z.-Q. Wu, J.-J. Xu, X.-H. Xia, H.-Y. Chen, Chem. Eur. J. 16 (2010) 10186–10194.
[8] J.Y. Lee, H.Y. Shin, S.W. Kang, C. Park, S.W. Kim, Biosens. Bioelectron. 26 (2011) 2685–2688.
[9] A.A. Karyakin, E.A. Kotel'nikova, L.V. Lukachova, E.E. Karyakina, J. Wang, Anal. Chem. 74 (2002) 1597–1603.
[10] J. Wang, Electroanalysis 13 (2001) 983–988.
[11] G.J. Moody, J.D.R. Thomas, Select. Electr. Rev. 13 (1991) 113–124.
[12] P.W. Stoecker, A.M. Yacynych, Select. Electr. Rev. 12 (1990) 137–160.
[13] L. Li, Q. Sheng, J. Zheng, H. Zhang, Bioelectrochemistry 74 (2008) 170–175.
[14] J. Zhu, Z. Zhu, Z. Lai, R. Wang, X. Guo, X. Wu, G. Zhang, Z. Zhang, Y. Wang, Z. Chen, Sensors 2 (2002) 127–136.
[15] H.N. Choi, M.A. Kim, W.Y. Lee, Anal. Chim. Acta 537 (2005) 179–187.
[16] M. Vaillancourt, J.W. Chen, G. Fortier, D. Belanger, Electroanalysis 11 (1999) 23–31.
[17] G. Lai, J. Wu, C. Leng, H. Ju, F. Yan, Biosens. Bioelectron. 26 (2011) 3782–3787.
[18] G. Cui, J.H. Yoo, J. Yoo, S.W. Lee, H. Nam, G.S. Cha, Electroanalysis 13 (2001) 224–228.
[19] J. Wang, F. Lu, L. Angnes, J. Liu, H. Sakslund, Q. Chen, M. Pedrero, L. Chen, O. Hammerich, Anal. Chim. Acta 305 (1995) 3–7.
[20] S. Liu, H.X. Ju, Biosens. Bioelectron. 19 (2003) 177–183.
[21] Y.H. Wu, S.S. Hu, Bioelectrochemistry 70 (2007) 335–341.
[22] K. Wang, Q. Liu, Q.-M. Guan, J. Wu, H.-N. Li, J.-J. Yan, Biosens. Bioelectron. 26 (2011) 2252–2257.
[23] A.P. Periasamy, Y.-J. Chang, S.-M. Chen, Bioelectrochemistry 80 (2011) 114–120.
[24] C. Deng, J. Chen, Z. Nie, S. Si, Biosens. Bioelectron. 26 (2010) 213–219.
[25] W. Chen, Y. Ding, J. Akhigbe, C. Brückner, C.M. Li, Y. Lei, Biosens. Bioelectron. 26 (2010) 504–510.
[26] X. Kang, Z. Mai, X. Zou, P. Cai, J. Mo, Anal. Biochem. 369 (2007) 71–79.
[27] L.J. Mi, X. Zhang, W.C. Yang, L.H. Wang, Q. Huang, C.H. Fan, J. Hu, J. Nanosci. Nanotechnol. 9 (2009) 2247–2255.
[28] G. Wang, J.J. Xu, H.Y. Chen, Electrochem. Commun. 4 (2002) 506–509.
[29] H.X. Ju, S.Q. Liu, B.X. Ge, F. Lisdat, F.W. Scheller, Electroanalysis 14 (2002) 141–147.
[30] C. Yang, J. Wu, Y. Hou, Chem. Commun. 47 (2011) 5130–5141.
[31] J.-D. Qiu, R.-P. Liang, X.-H. Xia, Biosens. Bioelectron. 25 (2010) 1447–1453.
[32] N. Zheng, W.Y. Yang, X.J. Li, Z.B. Yuan, Talanta 79 (2009) 780–786.

[33] C. Lu, Y. Hung, J. Hsiao, M. Yao, T. Chung, Y. Lin, S. Wu, S. Hsu, H. Liu, C. Mou, C. Yang, D. Huang, Y. Chen, Nano Lett. 7 (2007) 149–154.
[34] E. Katz, I. Willner, Angew. Chem. Int. Ed. 44 (2005) 4791–4794.
[35] J. Ge, Q. Zhang, T. Zhang, Y. Yin, Angew. Chem. Int. Ed. 47 (2008) 8924–8928.
[36] S.J. Guo, S.J. Dong, E.K. Wang, Chem. Eur. J. 15 (2009) 2416–2424.
[37] S. Si, C. Li, X. Wang, D. Yu, Q. Peng, Y. Li, Cryst. Growth Des. 5 (2005) 391–393.
[38] X. Wang, Z. Zhao, J. Qu, Z. Wang, J. Qiu, Cryst. Growth Des. 10 (2010) 2863–2869.
[39] K. Zhou, Y. Zhu, X. Yang, C. Li, New J. Chem. 34 (2010) 2950–2955.
[40] Y. Zhan, F. Meng, Y. Lei, R. Zhao, J. Zhong, X. Liu, Mater. Lett. 65 (2011) 1737–1740.
[41] J. Lu, X. Jiao, D. Chen, W. Li, J. Phys. Chem. C 113 (2009) 4012–4017.
[42] A. Yan, X. Liu, G. Qiu, N. Zhang, R. Shi, R. Yi, M. Tang, R. Che, Solid State Commun. 144 (2007) 315–318.
[43] V. Salgueiriño-Maceira, M.A. Correa-Duarte, M. Spasova, L.M. Liz-Marzán, M. Farle, Adv. Funct. Mater. 16 (2006) 509–514.
[44] A. Ulman, Chem. Rev. 96 (1996) 1533–1554.
[45] R. Wilson, Chem. Soc. Rev. 37 (2008) 2028–2045.
[46] H. Zhang, J.-J. Xu, H.-Y. Chen, J. Phys. Chem. C 112 (2008) 13886–13892.
[47] W. Stöber, A. Fink, E. Bohn, J. Colloid Interface Sci. 26 (1968) 62–69.
[48] W. Wu, Q.G. He, H. Chen, J.X. Tang, L.B. Nie, Nanotechnology 18 (2007) 145608–145609.
[49] J.-J. Feng, P. Hildebrandt, D.H. Murgida, Langmuir 24 (2008) 1583–1586.
[50] J.-J. Feng, U. Gernert, P. Hildebrandt, I.M. Weidinger, Adv. Funct. Mater. 20 (2010) 1954–1961.
[51] H. Deng, X. Li, Q. Peng, X. Wang, J. Chen, Y. Li, Angew. Chem. Int. Ed. 44 (2005) 2782–2785.
[52] R.G. Freeman, K.C. Grabar, K.J. Allison, R.M. Bright, J.A. Davis, A.P. Guthrie, M.B. Hommer, M.A. Jackson, P.C. Smith, D.G. Walter, M.J. Natan, Science 267 (1995) 1629–1632.
[53] D.P. Tang, R. Yuan, Y.Q. Chai, J. Phys. Chem. B 110 (2006) 11640–11646.
[54] K.R. Brown, D.G. Walter, M.J. Natan, J. Chem. Mater. 12 (2000) 306–313.
[55] J.A. Creighton, D.G.J. Eadon, J. Chem. Soc. Faraday Trans. 87 (1991) 3881–3891.
[56] J.L. Lyon, D.A. Fleming, M.B. Stone, P. Schiffer, M.E. Williams, Nano Lett. 4 (2004) 719–723.
[57] E. Katz, I. Willner, Electroanalysis 15 (2003) 913–947.
[58] E. Laviron, J. Electroanal. Chem. 100 (1979) 263–270.
[59] J.Z. Xu, J.J. Zhu, Q. Wu, Z. Hu, H.Y. Chen, Chin. J. Chem. 21 (2003) 1088–1091.
[60] J.B. Zheng, R.F. Gao, Electrochem. Commun. 11 (2009) 608–611.
[61] E. Laviron, J. Electroanal. Chem. 101 (1979) 19–28.
[62] S. Zhao, K. Zhang, Y. Bai, W. Yang, C. Sun, Bioelectrochemistry 69 (2006) 158–163.
[63] Z. Dai, G. Shao, J. Hong, J. Bao, J. Shen, Biosens. Bioelectron. 24 (2009) 1286–1291.
[64] Y. Huang, W. Zhang, H. Xiao, G. Li, Biosens. Bioelectron. 21 (2005) 817–821.
[65] C.Y. Deng, J.H. Chen, X.L. Chen, C.H. Xiao, L.H. Nie, S.Z. Yao, Biosens. Bioelectron. 23 (2008) 1272–1277.
[66] Y. Xiao, E. Katz, J.F. Hainfeld, I. Willner, Science 299 (2003) 1877–1881.
[67] R.A. Kamin, G.S. Wilson, Anal. Chem. 52 (1980) 1198–1205.